



Grain fragmentation and phase transformations in hafnium oxide induced by swift heavy ion irradiation

M. Dhanunjaya¹ · D. K. Avasthi² · A. P. Pathak¹ · S. A. Khan³ · S. V. S. Nageswara Rao¹

Received: 23 June 2018 / Accepted: 25 July 2018 / Published online: 6 August 2018
© Springer-Verlag GmbH Germany, part of Springer Nature 2018

Abstract

We report on the 100 MeV Ag ion irradiation-induced modifications in hafnium oxide films deposited by radio frequency (RF) magnetron sputtering method. The phase transformations and grain fragmentation within the films induced by ion irradiation have been investigated by employing grazing incident X-ray diffraction (GIXRD) and field emission scanning electron microscope (FESEM). The FESEM analysis confirms the grain fragmentation as function of ion fluence. The grain size varied from 70 to 15 nm with various irradiation fluences. The photoluminescence (PL) at 377 nm and 420 nm indicates the shallow oxygen defects and F-centers present in hafnium oxide films. After irradiation, the sharp peak at 377 nm disappears completely due to the ion-induced reconfiguration of defects. Sharp thermal gradients due to ion-induced electronic excitation can lead to the observed phase transformations and grain fragmentation in films. Particularly, the anisotropic thermal expansion in the nano-grains can cause grain fragmentation. Ion-induced defect annihilation, strain relaxation, phase transformation and grain fragmentation are interdependent processes and their mutual dependency is responsible for the observed changes in the films.

1 Introduction

Swift heavy ion (SHI) irradiation is a well-known and versatile technique to synthesize, characterize and modify the materials [1]. Ion beam irradiation is a very precise tool to create the interdiffusion in films, fabrication of the embedded nanoparticles (NPs) and to induce phase transformations [2–7]. During the passage of swift ions into the material or films, these ions deposit a huge amount of energy in the form of electronic and nuclear energy losses. This deposited high energy is initially absorbed by the electrons in the material, eventually gets transformed to lattice which leads to ion track formation, ion beam annealing, material modifications, etc. [8, 9]. There are several reports on material modifications such as amorphization, crystallization, amorphous to

crystalline transformations and crystalline to amorphous transformations [2–15].

Hafnium oxide (HfO₂) is a contemporary gate material having a wide range of research activity in the fields of both electronics and optoelectronics. A variety of properties such as high thermal stability on Si surface, wide bandgap (~5.7 eV), high dielectric constant (~25), high refractive index (~2) leads this material to replace the conventional gate dielectric material (SiO₂) in metal oxide semiconductor (MOS) devices [16]. High melting (2900 °C) and boiling (3500 °C) points make it a suitable refractory material in high-temperature applications [17, 18]. The better cytocompatibility eventually puts this material in the center stage in its applications for biosensors [16] and drug delivery in cancer therapy [19, 20]. The transparency of HfO₂ films is 80–90% for ultra-violet (UV) to the infra-red (IR) region, so that they can be used in bandpass filters, UV mirrors, astronomical charge-coupled devices (CCDs), anti-reflective multilayer coatings for night-vision devices and IR optical devices [21–25].

It is well known that the above-mentioned properties strongly depend on the phase, stoichiometry and surface morphology of the films. More importantly, the morphology is critical for sensing applications. Recent reports suggest that the phase and morphology can be engineered by

✉ S. V. S. Nageswara Rao
svnsp@uohyd.ac.in; nageshphysics@gmail.com

¹ School of Physics, University of Hyderabad,
Hyderabad 500046, India

² Amity Institute of Nanotechnology, Amity University, Noida,
Uttar Pradesh 201313, India

³ Inter-University Accelerator Centre, Aruna Asaf Ali Marg,
New Delhi 110067, India

employing SHI irradiation [26, 27]. However, the underlying mechanisms responsible for the observed phase and/or morphology change are still to be investigated in detail, which forms the basis for present work. Researchers have used various deposition techniques to synthesize the HfO_2 thin films. However, RF magnetron sputtering method is more frequently used for thin film depositions, because it is easy to fabricate the thin films, effectively at low cost compared to the other deposition techniques. The quality of the film, morphology, thickness of the deposited films can be tailored with deposition parameters such as deposition power, deposition pressure and deposition time. Our previous study suggests that the SHI irradiation can induce grain growth and amorphous to crystalline (monoclinic) transformation in thin HfO_2 films (~ 10 nm) deposited by RF sputtering at low RF powers [28]. In another study, Benyagoub [29] suggested crystalline to crystalline (monoclinic to tetragonal) in bulk HfO_2 under SHI irradiation. Here we present a study on the effects of SHI irradiation on the structural and surface properties of the considerably thick films of hafnium oxide (~ 500 nm).

2 Experimental details

Hafnium oxide films were deposited on Boron doped *p*-type Silicon (100) wafer with 1–10 Ω -cm resistivity substrates using RF magnetron sputtering method at room temperature. The Si substrates were cut into 1×1 cm² dimensions to get the uniformity while depositing the films. A commercially purchased 2-inch diameter and 3-mm-thick HfO_2 target having purity of 99.99% was used for film deposition. Silicon substrates were cleaned ultrasonically in deionized water (DIW), acetone, and isopropyl alcohol, each for 5 min and finally these substrates were rinsed with DIW thoroughly. After completing the cleaning process, the substrates were immediately clamped to the substrate holder and substrate holder was loaded into the sputtering chamber. Initially, the sputtering chamber was evacuated to a base pressure of 9×10^{-6} mbar with the help of turbo molecular pump backed by a roughing pump. After reaching the above-mentioned base pressure, a 20 standard cubic centimeters per minute (SCCM) of 99.99% pure argon (Ar) gas was introduced into the sputtering chamber using mass flow controller (MFC). The prior depositions were carried out at a pressure of 2.4×10^{-3} mbar. The target to substrate distance was maintained at 12.5 cm. A 120-W RF power was used to deposit the films and deposition was carried out for 4 h of time to get the thicker films. While depositing the films, the substrate rotation (10 rpm) was used throughout the deposition for uniformity. The pre-estimated thickness was 500 nm. Ambios XP 200 Profilometer was used to

measure the deposited film thickness, and it was estimated to be around 475 nm.

The deposited thick HfO_2 films on Si substrates were subjected to 100 MeV Ag^{7+} SHI irradiation using a 15 UD tandem Pelletron accelerator at Inter-University Accelerator Centre (IUAC), New Delhi. The range and energy loss of ions in HfO_2 were estimated using stopping and range of ions in matter (SRIM-2013) simulation code [30]. The calculated ion range (R), electronic energy loss (S_e) and nuclear energy loss (S_n) for 100 MeV Ag ions in HfO_2 were estimated to be 7.7 μm , 23.2 keV/nm and 0.15 keV/nm, respectively. The hafnium oxide film thickness was around 500 nm which is small compared to the projected ion range 7.7 μm . The ion beam was scanned over 1×1 cm² of the sample area at a constant beam current of 1 particle nano-Ampere (pnA) to avoid the heating up of substrates. The ion fluence was varied from 3×10^{12} to 1×10^{14} ions/cm² by varying the irradiation time.

The pristine and SHI-irradiated films were characterized using different techniques. Field emission scanning electron microscope (FE-SEM: Carl ZEISS, FEG, ultra-55) was used to scan the surface morphology, evolved grains and to measure the film thickness from the cross-sectional image. Bruker D8 Advance diffractometer with Cu K_α source ($\lambda = 0.154$ nm) was used to estimate the possible phase changes in films. Photoluminescence (PL) measurements were performed using Fluorolog, Xenon lamp, 450 W, having a resolution of 0.3 nm. Rutherford backscattering spectroscopy (RBS) measurements have been performed on the sample to estimate the composition and thickness of films. These measurements were performed using 2 MeV He^{2+} ions at a scattering angle of 165° at IUAC, New Delhi. The SIMNRA-7.01 [31] was used to simulate the acquired RBS spectra.

3 Results and discussion

Thick HfO_2 films deposited by RF magnetron sputtering were studied before and after irradiation by various characterization techniques. Initially, the film thickness was measured from Ambios XP 200 Profilometer, and it was determined to be around 475 nm. Later, the RBS measurement was also performed to estimate the thickness and composition of films. Calibration offset and energy per channel were estimated to be 96 keV and 0.961 keV/ch, respectively, using a calibration sample (Au/SiO_2), to simulate the RBS spectrum shown in Fig. 1. The estimated areal density is 2550×10^{15} atoms/cm³ which is equal to 430 nm of film thickness assuming the standard density of HfO_2 and film composition was found to be around $\text{HfO}_{2.7}$. Inset of Fig. 1 depicts the cross-sectional FESEM image of the pristine sample and it indicates a film thickness of 460 nm, which

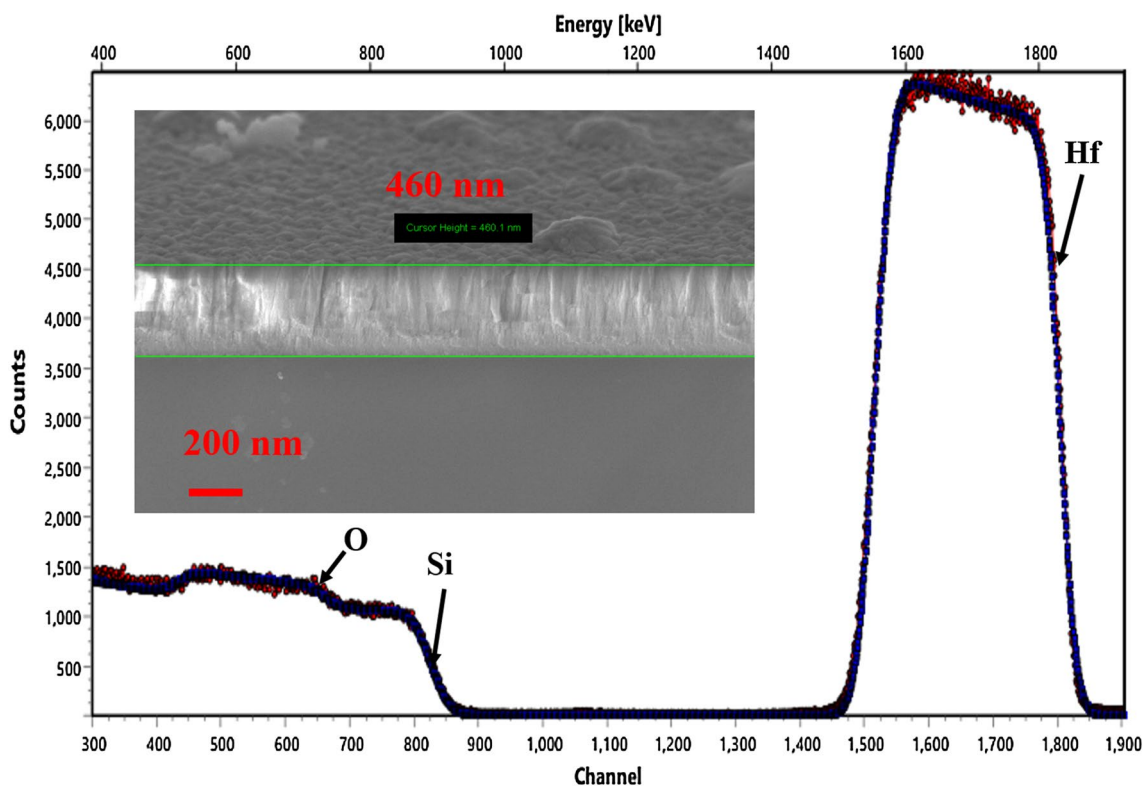


Fig. 1 RBS spectrum of as-deposited HfO_2 thick film. Solid line indicates the fit obtained by SIMNRA simulation (inset shows the cross-sectional FESEM image). Measured film thickness is 460 nm as shown in the inset

is in agreement with the nominal value of 500 nm and with measured values from profilometer and RBS measurements.

3.1 Surface morphology and grain fragmentation

The microstructure, surface morphology, and the development of grain sizes of the films are studied using the FESEM measurements. The pristine and SHI-irradiated HfO_2 films have been studied using 5 kV extra-high-tension (EHT) electron gun at different magnification levels. The FESEM image of the pristine sample is shown in Fig. 2. The surface image of the pristine sample shows the elongated nano-flake-like structures, and the average nano-flake size is around 70 nm along its long axis and width of the nano-flake varied from 20 to 30 nm. The first analysis confirmed that the film morphology and the grain (nano-flake) size depends on the RF magnetron sputtering deposition parameters, such as deposition power and deposition pressure, when compared to previous reports [28, 32–34]. On closer observation, we notice non-uniform, inhomogeneous and irregular grains at higher deposition rates, which is consistent with irregular columnar grain growths of other materials [35]. Looks like each of the large grain is a combination of smaller grains each around 15 nm size. In general, this type of morphology is less dense, loosely packed and corresponds to highly

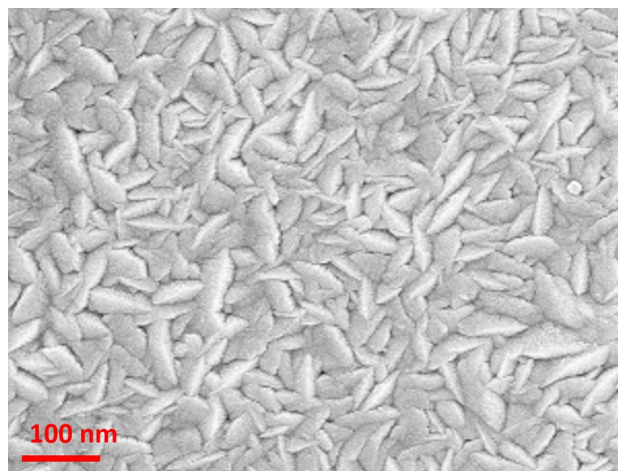


Fig. 2 FESEM image of the surface of the pristine HfO_2 films deposited by RF magnetron sputtering at 120 W

strained structures [36]. The adhesion between the grains in the film is very poor.

After SHI irradiation at different ion fluences, the film surface morphology and grain size change completely as shown in Fig. 3a–d. Upon irradiation with a fluence of 3×10^{12} ions/cm², the large flake-structured grains started destabilizing

Fig. 3 FESEM images of HfO₂ thick films as a function of fluence: **a** fluence 3×10^{12} ions/cm², **b** fluence 1×10^{13} ions/cm², **c** fluence 3×10^{13} ions/cm² and **d** fluence 1×10^{14} ions/cm²

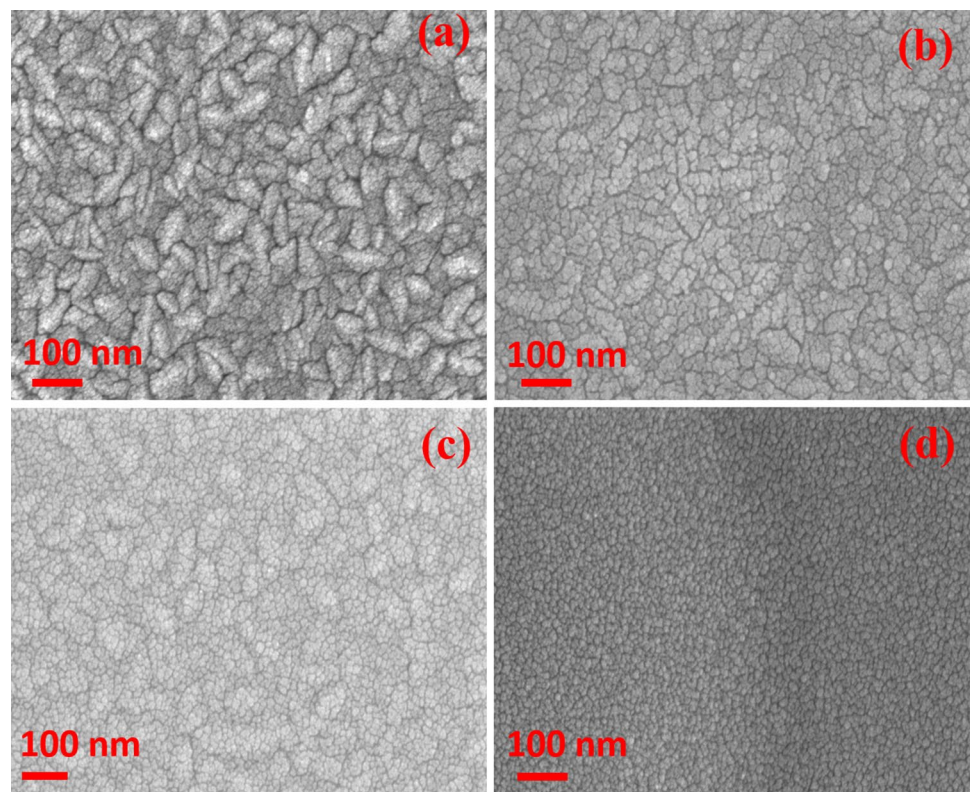


Table 1 Sample name, ion fluence, grain sizes estimated by various methods

Sample name	Irradiation fluence (ions/cm ²)	Particle/grain size (nm) estimated by	
		GIXRD (nm)	FESEM (nm)
HfO ₂ /Si-1	Pristine	62	70
HfO ₂ /Si-2	3×10^{12}	48	60
HfO ₂ /Si-3	1×10^{13}	32	35
HfO ₂ /Si-4	3×10^{13}	22	26
HfO ₂ /Si-5	1×10^{14}	14	15

without any change in flake structure, and average flake size was around 60 nm along its long axis. Further, an increase of fluence to 1×10^{13} ions/cm², the evolution of new grains started within the flack structure. The destabilization of grains was slightly higher when compared to the previous fluence. At this fluence, the grain size was around 35 nm along its long axis. On further increasing the fluence to 3×10^{13} ions/cm², the flake structure was destroyed completely, and the formation of individual sphere-like grains of size 25–30 nm started. At highest fluence of 1×10^{14} ions/cm², the surface is further smoothed with uniform average grain size of 15 nm. The grain size variation with ion fluence is summarized in Table 1 and Fig. 5. The main reason behind the change of grain size and morphology can be understood in terms of the phenomena

of ion-induced grain fragmentation within the film. There are some reports in the literature on ion-induced grain fragmentation in fluoride thin films [37–39]. The strained nano-grains or nano-flakes are expected to be relaxed during SHI irradiation to promote grain fragmentation process and phase transitions in films. Hence, the ion-induced electronic energy loss within the film plays a major role in observed grain fragmentation and morphological changes. This study exhibits an important property, ion-induced smoothing of surfaces, of SHI irradiation.

3.2 Phase transformations and crystallinity

Pristine and 100 MeV Ag ion-irradiated HfO₂ films were studied by GIXRD measurement and the results are shown in Fig. 4. All the films were scanned over 20°–80° of 2θ and grazing angle was kept at 4°. The peaks in the diffraction patterns of pristine samples centered at 2θ values of 24.16° and 34.30° correspond to the (011) and (020) crystal planes, respectively. These crystal planes were assigned to the monoclinic phase of HfO₂ by matching with the standard JCPDS file (PDF# 06-0318) having space group of P2₁/c. The average crystallite size has been calculated using Scherrer's formula [40] as given below:

$$d = \frac{0.9\lambda}{\beta \cos \theta} \quad (1)$$

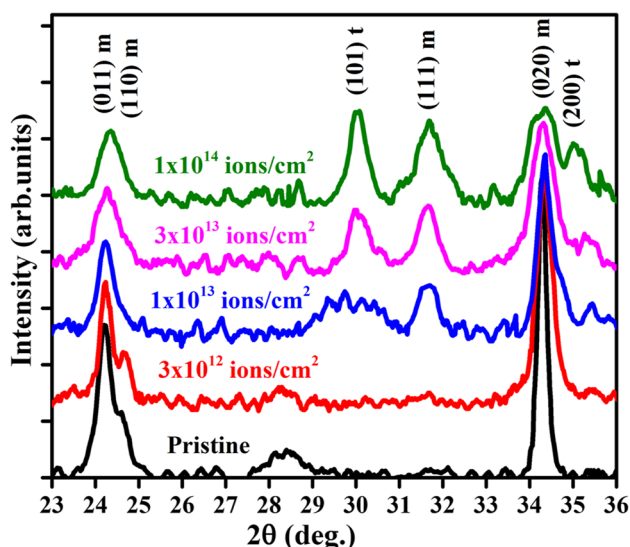


Fig. 4 GIXRD patterns of both pristine and irradiated HfO₂ films deposited on Si substrates (each graph is labeled with corresponding fluence)

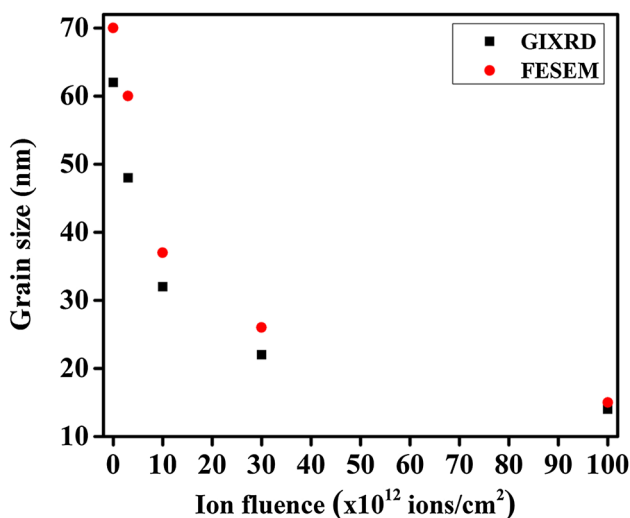


Fig. 5 Grain size estimated by GIXRD and FESEM measurements

where ‘λ’ is the wavelength of X-rays (1.54 Å), ‘β’ is full width half maximum, ‘θ’ is Bragg’s angle. Initially, the grain size was around 62 nm, and after SHI irradiation the grain size decreases drastically with the ion fluence, as shown in Table 1 and Fig. 5.

Along with the decrease in grain size, a fractional phase change was observed after irradiation of these samples with 100 MeV Ag⁷⁺ ion. The new peak located at 2θ = 30.04° in irradiated samples corresponds to the tetragonal phase of the crystal plane (101) as per the standard JCPDS file (PDF# 00-008-0342). The intensity of this tetragonal peak is found to increase with increase in the ion fluence. The tetragonal

phase was not observed for pristine or even for low-dose samples (up to an ion fluence of 3 × 10¹² ions/cm²). This phase change was significant for the ion fluences 1 × 10¹³, 3 × 10¹³ and 1 × 10¹⁴ ions/cm². A new tetragonal peak corresponding to (200) planes emerged at 2θ = 35.09° for highest fluence. The fraction of phase change is calculated using Garvie and Nicholson [41] equation as given below:

$$C_t = \frac{I_t(101)}{I_m(011) + I_t(101) + I_m(020)} \quad (2)$$

where ‘C_t’ is the compositional weight of tetragonal phase, ‘I_m’, ‘I_t’ are integral areas of the monoclinic and tetragonal phases (or intensities of corresponding peaks). C_m (= 1 – C_t) gives the monoclinic compositional weight. The calculated fractional tetragonal phase with ion fluence is shown in Fig. 6. The maximum tetragonal phase of 35% was attained for the ion fluence of 1 × 10¹⁴ ions/cm². SHI-induced crystalline to crystalline phase transitions were earlier observed in bulk ZrO₂ and HfO₂ [29, 42–44]. Monoclinic to tetragonal transition was induced in ZrO₂ and HfO₂ by 595 MeV Xe and 295 I ion irradiations, respectively. These results are consistent with the present 100 MeV Ag ion irradiation-induced phase transitions in 500 nm HfO₂ films deposited by RF magnetron sputtering.

Along with the evolution of tetragonal phase, the intensity of dominant monoclinic phase peaks [for (011) and (020) in pristine sample] decreased with the increase in ion fluence. An increase in the width of these peaks is also observed. Initially, the grain size was 62 nm which further decreased to 15 nm with increase in ion fluence. The decrease in grain size, decrease in peak area and increase in peak width with ion fluence may be attributed to the ion-induced grain fragmentation

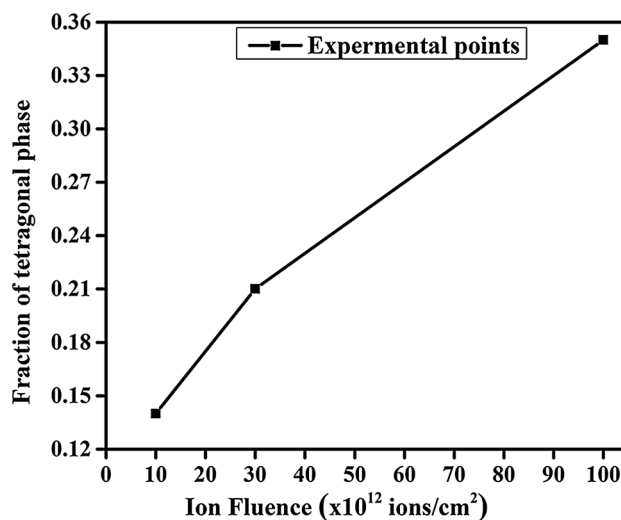


Fig. 6 Fraction of tetragonal phase with respect to monoclinic phase as a function ion fluence in HfO₂ films

process. Similar results have been observed in other thin films by various groups [38, 39] and an appropriate method was proposed to estimate the corresponding track radius by GIXRD analysis. To determine the track radius from the GIXRD data, peaks were normalized and averaged with the dominant peak for the pristine sample. The obtained values were fitted using exponential Poisson's equation as given below [38] to determine damage cross sections along different crystallographic directions:

$$A(\phi t) = (1 - S_a) \times \exp(-\sigma_a \times \phi t) + S_a \quad (3)$$

where $A(\phi t)$ is normalized area of the concerned peak at given fluence, S_a is the saturated normalized area at highest fluence, σ_a is the damage cross section along the corresponding crystallographic direction. The increase in intensity appears to be linear at lower fluences with slope I_a of the fitting is equal to the $-\sigma_a \times (1 - S_a)$. From this slope, we can deduce the information of track radius ($\sigma_a = \pi \times r^2$). The initial slopes of the corresponding peaks are -21.1 (020), -36.27 (011), followed by damage cross sections as 43.7 (020), 75 (011) nm^2 . The corresponding track radii deduced from peak areas were 3.7 nm along (020) direction and 4.9 nm along (011) direction. The damage cross section and track diameters are found to be different along different crystallographic directions which can result in uneven thermal expansion leading to the observed grain fragmentation. The fitted exponential Poisson's graph is shown in Fig. 7. Consequently, the width of the diffraction peak increases with the decrease of the peak area. The widths of the normalized peaks are averaged with the pristine sample and fitted with the Poisson's exponential fitting and are given by [38]

$$W(\phi t) = S_w(1 - \exp(-\sigma_w \times \phi t)) + 1 \quad (4)$$

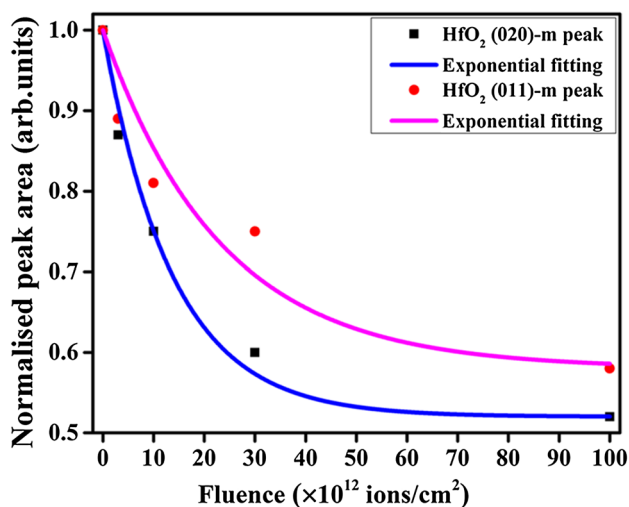


Fig. 7 Normalized peak areas of dominant peaks with respect to pristine sample as a function of ion fluence

where $W(\phi t)$ is normalized peak width at a given fluence, S_w is the saturated normalized width at highest fluence and σ_w is the damage cross section. The initial slope I_w of the fitting is equal to the $\sigma_w \times S_w$. From this slope, we can deduce the information about track radius ($\sigma_a = \pi \times r^2$). The initial slopes of the corresponding peaks are 30.5 (020), 33.5 (011) and followed by damage cross sections as 17.9 (020), 22.3 (011) nm^2 . The corresponding track radii deduced from peak widths were 2.4 nm along (020) direction and 2.7 nm along (011) direction. The fitted exponential Poisson's graph is shown in Fig. 8. From the two fittings, the extracted track radii by these two methods are in agreement with each other. Overall, the estimated average track radii are in the range of $5\text{--}7$ nm. However, here it is important to note that the prediction of non-symmetric tracks along ion paths owing to the anisotropy of thermal properties of HfO_2 along different planar directions. This confirms the significance of thermal spike and consequent effects in the material modification by SHI irradiation.

3.3 Ion-induced reconfiguration and annihilation of defects

The PL measurements were performed on pristine and irradiated samples to monitor the dynamics of defect states as a function of fluence. The excitation wavelength was 350 nm. The HfO_2 bandgap is around 5.7 eV, which is much higher than the excitation energy 3.55 eV. Hence, the observed PL from the HfO_2 is attributed to the transition from mid-band-gap states or defect states within the excitation energy range. The PL spectra of both pristine and SHI-irradiated samples are shown in Figs. 9 and 10. The pristine sample has shown a dominant peak at 377 nm (3.3 eV), and a broad peak from

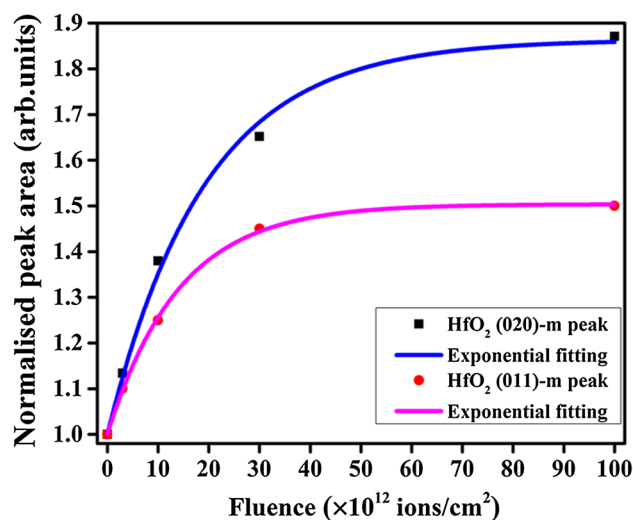


Fig. 8 Normalized peak widths of dominant peaks with respect to pristine sample as a function of ion fluence

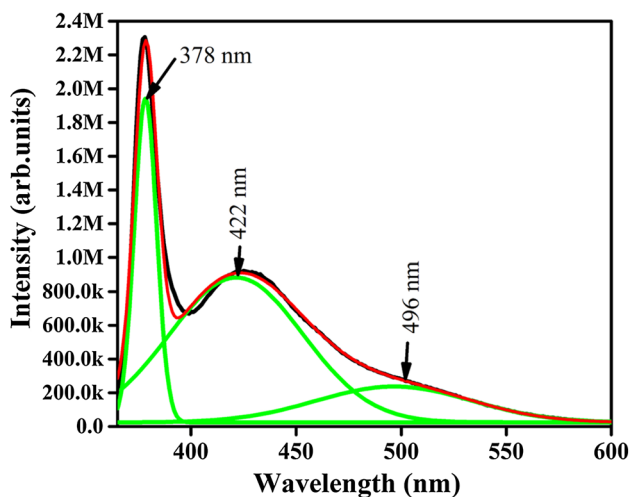


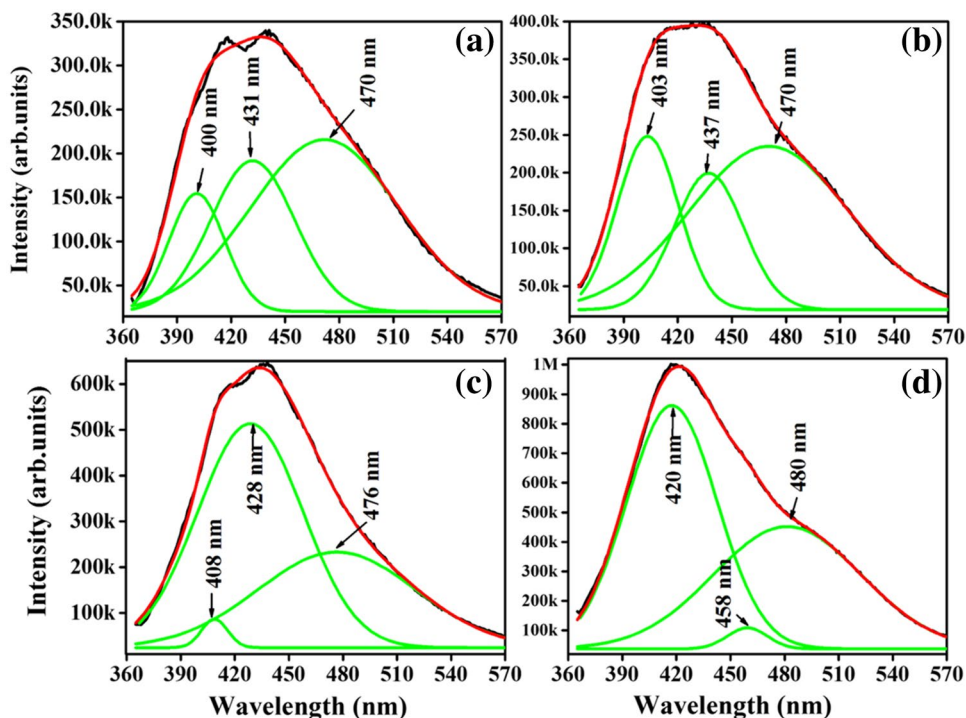
Fig. 9 PL spectra of pristine HfO₂ film (curves obtained by de-convolution are also shown)

400 to 550 nm in the visible region. After deconvolution using peak fitting program, the broad peak yields the new peaks at 2.93 eV and 2.5 eV. Most of the literature suggests that PL originates from the oxygen-related vacancy defects in HfO₂. The emission in the HfO₂ may be understood as follows: the excitation energy was 3.5 eV, the electrons in the valence band get excited up to 3.5 eV above the valence band and relaxed to the defect states via radiative transition and the relaxed carriers combined with the holes in the valence band via emission. Hf-related defects are not

detectable in the PL experimental setup. Under the influence of SHI irradiation, the sharp dominant peak at 377 nm disappears completely for all the fluences, and only the broad peak remains intact. The single neutral oxygen vacancy can be distributed over the bandgap, but maxima are localized at 377 nm (3.3 eV) [45]. Wen et al. [46] reported that peaks at 2.71 eV and 2.94 eV belong to the positively charged oxygen vacancy states of Vo²⁺ and Vo⁺.

After ion irradiation, the neutral oxygen vacancies are suppressed completely. All of these defects depend on the deposition parameters. In general, the defects can be expected in suboxide formation (HfO_x, x < 2) which is consistent with our RBS analysis. Approximately, the broad peak position is the same for all irradiated samples except for minor increase in intensity. The shift in the PL emission band to the higher wavelength side believed to be due to change in the stress/strain in the HfO₂ films, which is generated from the change in the crystal phase from monoclinic to tetragonal [47]. After deconvolution using peak fitting program, each peak is clearly seen to be a combination of 3.0 eV, 2.9 eV, and 2.6 eV as shown Fig. 10a–d. In our recent reports, we noticed the similar kind of results in thin (~ 10 nm) HfO₂ films [28, 32]. Most of these shallow and deep-level emissions in HfO₂ may be attributed to oxygen-related intrinsic defect states in between the conduction and valence band states or F-centers [48]. When the material transforms from one phase to another phase, some of the defects may disappear while other types of defects remain intact due to inevitable changes in the strains

Fig. 10 PL spectra of HfO₂ thick films: **a** fluence 3 × 10¹² ions/cm², **b** fluence 1 × 10¹³ ions/cm², **c** fluence 3 × 10¹³ ions/cm², **d** fluence 1 × 10¹⁴ ions/cm². X-axis indicates the wavelength (nm), Y-axis indicates the intensity (arb. units). The curves obtained by de-convolution are also shown



during these phase transitions. 2.7 eV blue luminescence has been reported by various research groups in HfO₂ and this defect state slightly shifted from 2.6 to 2.8 eV upon irradiation [49]. 3.1 eV defect peak might be associated with the charged oxygen defect state [50]. The change in defect configurations indicates the changes in the strain due to SHI irradiation which is consistent with the observed grain fragmentation and phase transformations in these films. The schematic representation of the estimated defect states and their tentative assignment are shown in Fig. 11 and Table 2, where, B1, B2, B3 and B4 are radiative transitions from the excited level to the defect states [51]. Further, the observable minor changes in the peak position of various peaks in the GIXRD patterns (shown in Fig. 5) with increase in

fluence also indicates the ion-induced changes in the strains in samples. The introduction of a tetragonal phase within a film of monoclinic phase demands the change in strain configuration. This is consistent with the observed PL and GIXRD results.

3.4 Thermal spike model and conclusions

There are few reports on ion-induced amorphous to crystalline, crystalline to amorphous and crystalline to crystalline transformations in ZrO₂ and HfO₂ [28, 29, 43]. ZrO₂ and HfO₂ are twin oxides and both exhibit almost similar properties. The monoclinic phase of HfO₂ can exist from room temperature to 1700 °C, whereas in the case of ZrO₂ it is from room temperature to 1100 °C. The tetragonal phase of HfO₂ is stable from 1700 to 2500 °C whereas for ZrO₂ it is around 1100–2200 °C, respectively. With further increase in temperature, both twin oxides transform to cubic phase. While transforming from monoclinic to tetragonal phase, there is a change in volume fraction of HfO₂ by 3.5% [52]; however, compared to ZrO₂ (7.5%), it is very small [52]. The volume expansion coefficient is different for different crystallographic directions for HfO₂ which can cause the observed grain fragmentation during SHI irradiation. Associated with uneven thermal expansion in HfO₂ nano-grains, one can expect the grain fragmentation. In another context, the rapid increase of temperature leads to the thermal shock wave in the film. The thermal shock wave creates enough pressure to cripple the nano-grains and leads to the grain fragmentation.

The newly formed grain size purely depends on the thermal contraction rate and strain relaxation in large grains. The

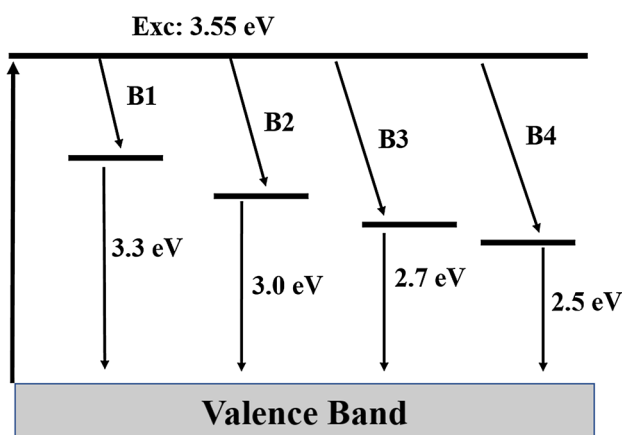


Fig. 11 Schematic diagram of light emission from the defects states of the HfO₂ films (tentative predictions from the PL data)

Table 2 Observed emission wavelengths and tentative assignment of emission peaks

S. no.	Sample name	Composition	Observed PL peak position (nm)	Tentative defect assignment	Reference used for assignments
1	HfO ₂ /Si-1	Hf _{0.27} O _{0.73}	378 (~3.3 eV)	Vo	[45–48]
			422 (2.9 eV)	Vo ⁺	
			496 (2.5 eV)	–	
2	HfO ₂ /Si-2	Unknown	400 (3.1 eV)	–	
			431 (2.9 eV)	Vo ⁺	
			470 (2.6 eV)	–	
3	HfO ₂ /Si-3	Unknown	403 (3.1 eV)	–	
			437 (2.8 eV)	–	
			470 (2.6 eV)	–	
4	HfO ₂ /Si-4	Unknown	408 (3.0 eV)	–	
			428 (2.9 eV)	Vo ⁺	
			476 (2.6 eV)	–	
5	HfO ₂ /Si-5	Unknown	420 (2.9 eV)	Vo ⁺	
			458 (2.7 eV)	Vo ²⁺	
			480 (2.6 eV)	–	

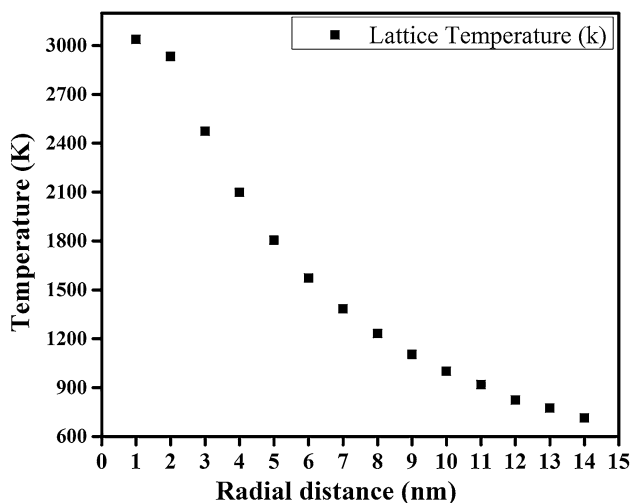


Fig. 12 Evolution of lattice temperature with radial distance from ion path in HfO_2 films estimated by thermal spike model

rapid phase transformation is also responsible for the grain fragmentation. This anomaly can be observed in multiphase ceramics such as HfO_2 , ZrO_2 , AlO_3 [53]. The grain fragmentation mainly depends on the initial grain size and strain generated within the grains [54, 55]. In this process, the grain size reduces to a critical size after strain relaxation. In the other context, the bulk free energy per unit volume (G_b) in *m*- HfO_2 is the lowest and in the case of tetragonal- HfO_2 it is the highest. The surface free energy per unit volume (γ) for *t*- HfO_2 is the lowest and in the case of monoclinic HfO_2 , it is the highest [56]. When the phase transition takes place between the two stable phases (*m* to *t*) the grain size decreases to a stabilized minimum grain size [56]. Along with that there are few models explaining the grain fragmentation [57, 58].

The electronic energy loss of 23.2 keV/nm is deposited within the HfO_2 film under 100 MeV Ag ion irradiation. This huge amount of deposited energy can bring the material to the melting temperatures within the fraction of picosecond timescales in confined areas. The calculated atomic temperature as a function of radial distance at time [37] is shown in Fig. 12. The phase transformation of material happens when the temperature reaches the phase transition temperature. According to thermal spike calculations, the track radius is around 5–7 nm which indicates the rise in temperature is equal to the tetragonal phase transformation temperature. The rise in temperature in the damaged cross section area and calculated track radius are compatible with each other. In the process, thermal gradient-induced shock wave pressure cripples the strained nano-grains or nano-flakes. However, it is important to note that these high temperatures are not reached in thin (~ 10 nm) nano-structured films studied in our previous report [28]. The estimated track

size is also less in thicker films. Moreover, the track size is different along different crystallographic directions owing to the anisotropy of thermal properties in this material. The observed phase changes, grain fragmentation, defects creation or annihilation are inter-dependent under certain critical conditions. Hence, several manifestations of SHI irradiation are observed in this work. These results once again confirm the role of transient thermal spike during SHI irradiation and significance of thermal spike model in analyzing ion–solid interactions.

4 Conclusions

Films of hafnium oxide were deposited on Si substrates by RF magnetron sputtering method at high RF power (120 W). The thickness of the as-grown films was around 500 nm and they exhibit monoclinic phase. The obtained self-oriented nano-flake structures are attributed to high deposition rates and film growth conditions. After 100 MeV SHI irradiation, phase transformation, grain fragmentation and defect annihilation have been observed as a function of ion fluence. Ion-induced track radius is calculated within the films by studying the changes in peak areas and peak widths of various peaks observed in the GIXRD patterns. The average track radii are estimated to be 3–4.5 nm and the corresponding calculated atomic temperatures reached the critical value for tetragonal phase transformation temperature. FESEM data confirm the ion-induced grain fragmentation. PL emission at 377 nm and broad emission at 420 nm indicate the shallow oxygen defects and F centers present in the as-grown hafnium oxide films. After irradiation, the sharp peak at 377 nm disappears completely. Ion-induced heat desorption and anisotropic thermal expansion in the nano-grains are expected to cause the observed grain fragmentation. Electronic energy loss-induced sharp rise of thermal gradient is the most likely cause of the phase transformation in the film. Ion-induced defect annihilation, strain relaxation and defragmentation are found to be interdependent phenomena.

Acknowledgements MD and SVN thank IUAC for financial support through UFR project. We thank Mr. Sunil Ojha, IUAC, for his support in RBS measurements and analysis.

References

1. E. Zarkadoula, M. Toulemonde, W.J. Weber, *Appl. Phys. Lett.* **107**, 261902 (2015)
2. J.C. Pivin, G. Roger, M.A. Garcia, F. Singh, D.K. Avasthi, *Nucl. Instrum. Methods Phys. Res. B* **215**, 373–384 (2004)
3. M.C. Ridgway, R. Giulian, D.J. Sprouster, P. Kluth, L.L. Araujo, D.J. Llewellyn, A.P. Byrne, *Phys. Rev. Lett.* **106**, 095505 (2011)
4. S.A. Khan, D.K. Avasthi, S. Hooda, *Appl. Phys. A* **124**, 351 (2018)

5. H. Amekura, S. Mohapatra, U.B. Singh, S.A. Khan, P.K. Kulriya, N. Ishikawa, N. Okubo, D.K. Avasthi, *Nanotechnology* **25**, 435301 (2014)
6. U.B. Singh, D.C. Agarwal, S.A. Khan, S. Mohapatra, A. Tripathi, D.K. Avasthi, *J. Phys. D Appl. Phys.* **45**, 445304 (2012)
7. N. Srinivasa Rao, A.P. Pathak, N. Sathish, G. Devaraju, S.A. Khan, K. Saravanan, B.K. Panigrahi, K.G.M. Nair, D.K. Avasthi, *Nucl. Instrum. Methods Phys. Res. B* **268**, 1741–1743 (2010)
8. G.S. Virdi, B.C. Pathak, D.K. Avasthi, D. Kanjilal, *Nucl. Instr. Methods Phys. Res. B* **187**, 189–200 (2002)
9. G. Szenes, *Phys. Rev. B* **51**, 8026 (1995)
10. A.P. Pathak, N.S. Rao, G. Devaraju, V. Saikiran, S.V.S. Nageswara Rao, *MRS Bull.* **1354**, 79–90 (2011)
11. V. Saikiran, V.S. Vendamani, S. Hamad, S.V.S. Nageswara Rao, S. Venugopal Rao, A.P. Pathak, *Nucl. Instrum. Methods Phys. Res. B* **333**, 99–105 (2014)
12. S.V.S. Nageswara Rao, V.S. Vendamani, S.K. Satrasala, S.K. Padhe Srinadha Rao, K.S. Dhamodaran, A.P. Pathak, *AIP Conf. Proc.* **1336**, 332–336 (2011)
13. A. Biswas, R. Gupta, N. Kumar, D.K. Avasthi, J.P. Singh, S. Lotha, D. Fink, S.N. Paul, S.K. Bose, *Appl. Phys. Lett.* **78**, 4136 (2001)
14. K. Jeet, V.K. Jindal, L.M. Bharadwaj, D.K. Avasthi, K. Dharamvir, *J. Appl. Phys.* **108**, 034302 (2010)
15. S.K. Gautam, A. Chettah, R.G. Singh, S. Ojha, F. Singh, *Nucl. Instrum. Methods Phys. Res. B* **379**, 224–229 (2016)
16. J. Larkin, R. Henley, D.C. Bell, T. Cohen-Karni, J.K. Rosenstein, M. Wanunu, *ACS Nano*. **7**, 10121 (2013)
17. J.F. Justin, A. Jankowiak, *J. Aerosp. Lab.* **3**, 1–11 (2011)
18. E.P. Simonenko, D.V. Sevast'yanov, N.P. Simonenko, Sevast'yanov VG, Kuznetsov NT, *Russ. J. Inorg. Chem.* **58**, 1669–1693 (2013)
19. M. Lee, N. Zine, A. Baraket, M. Zabala, F. Campabadal, R. Caruso, M.G. Trivella, N.J. Renault, A. Errachid, *Sens. Actuator B Chem.* **175**, 201–207 (2012)
20. L. Maggiorella, G. Barouch, C. Devaux, A. Pottier, E. Deutsch, J. Bourhis, E. Borghi, L. Levy, *Future Oncol.* **8**(9), 1167–1181 (2012)
21. M. Fadel, O.A. Azim, M.O.A. Omer, R.R. Basily, *Appl. Phys. A* **66**, 335–343 (1998)
22. J. Niinistö, K. Kukli, M. Heikkilä, M. Ritala, M. Leskela, *Adv. Eng. Mater.* **11**, 223–234 (2009)
23. C. Wiemer, L. Lamagna, S. Baldovino, M. Perego, S. Schamm-Chardon, P.E. Coulon, O. Salicio, G. Congedo, S. Spiga, M. Fanciulli, *Appl. Phys. Lett.* **96**, 18290 (2010)
24. V. Pervak, F. Krausz, A. Apolonski, *Thin Solid Films* **515**, 7984–7989 (2007)
25. J.D. Traylor Kruschwitz, W.T. Pawlewicz, *Appl. Opt.* **36**, 2157–2159 (1997)
26. T. Tan, Z. Liu, H. Lu, W. Liu, H. Tian, *Opt. Mat.* **32**, 432–435 (2010)
27. S.K. Singh, R. Singhal, R. Vishnoi, V.V.S. Kumar, P.K. Kulriya, *Indian. J. Phys.* **91**, 547–554 (2017)
28. M. Dhanunjaya, S.A. Khan, A.P. Pathak, D.K. Avasthi, S.V.S. Nageswara Rao, *J. Phys. D Appl. Phys.* **50**, 505301 (2017)
29. A. Benyagoub, *Phys. Rev. B* **72**, 094114 (2005)
30. J.F. Ziegler, SRIM-2003. *Nucl. Instrum. Methods B.* **1027**, 219–220 (2004)
31. M. Mayer, SIMNRA: simulation of RBS, ERD and NRA spectra. *AIP Conf. Proc.* **475**, 541 (1999). <http://www.rzg.mpg.de/mam>. Accessed 6 Aug 2018
32. N. Manikantababu, M. Dhanunjaya, S.V.S. Nageswara Rao, A.P. Pathak, *Nucl. Instr. Meth. Phys. Res. B* **379**, 230–234 (2016)
33. N. Manikantababu, N. Arun, M. Dhanunjaya, S.V.S. Nageswara Rao, A.P. Pathak, *Radiat. Eff Defects Solids* **171**, 77–86 (2016)
34. M. Dhanunjaya, N. Manikantababu, A.P. Pathak, S.V.S. Nageswara Rao, *AIP Conf. Proc.* **1731**, 080071 (2016)
35. A.M. Hofer, J. Schlacher, J. Keckes, J. Winkler, C. Mitterer, *Vacuum*. **99**, 149–152 (2014)
36. X. Dai, A. Zhou, L. Feng, Y. Wang, J. Xu, J. Li, *Thin Solid Films* **567**, 64–71 (2014)
37. M. Kumar, R.K. Pandey, P. Rajput, S.A. Khan, F. Singh, D.K. Avasthi, A.C. Pandey, *J. Alloy Compd.* **695**, 83–90 (2017)
38. M. Toulemonde, A. Benyagoub, C. Trautmann, N. Khalfaoui, M. Boccanfuso, C. Dufour, F. Gourbilleau, J.J. Grob, J.P. Stoquert, J.M. Costantini, F. Haas, E. Jacquet, K.O. Voss, A. Meftah, *Phys. Rev. Lett.* **85**, 054112 (2012)
39. M. Kumar, R.K. Pandey, P. Rajput, S.A. Khan, U.B. Singh, D.K. Avasthi, A.C. Pandey, *Phys. Chem. Chem. Phys.* **19**, 23229 (2017)
40. P. Scherrer, *Göttinger Nachr. Gesell.* **2**, 98 (1918)
41. R.C. Garvie, P.S. Nicholson, *J. Am. Ceram. Soc.* **55**, 303–305 (1972)
42. H.S. Lokesh, K.R. Nagabhushana, F. Singh, *J. Alloy Compd.* **647**, 921–926 (2015)
43. H.S. Lokesh, K.R. Nagabhushana, F. Singh, *Nucl. Instrum. Methods Phys. Res. B* **379**, 131–135 (2016)
44. A. Benyagoub, *Eur. Phys. J. B* **34**, 395–398 (2003)
45. T.V. Perevalov, V. Sh. Aliev, V.A. Gritsenko, A.A. Saraev, V.V. Kaichev, *Microelectron. Eng.* **109**, 21–23 (2013)
46. R.-T. Wen, L.-S. Wang, H.-Z. Guo, Y. Chen, G.-H. Yue, D.-L. Peng, T. Hihara, K. Sumiyama, *Mater. Chem. Phys.* **130**, 823–826 (2011)
47. L. Kumari, W.Z. Li, J.M. Xu, R.M. Leblanc, D.Z. Wang, Y. Li, H. Guo, J. Zhang, *Cryst. Growth Des.* **9**, 3874–3880 (2009)
48. D.R. Islamov, V.A. Gritsenko, T.V. Perevalov, *ECS Trans.* **69**, 197–203 (2015)
49. V.A. Gritsenko, T.V. Perevalov, D.R. Islamov, *Phys. Rep.* **613**, 1–20 (2016)
50. T.V. Perevalov, D.V. Gulyaev, V.S. Aliev, K.S. Zhuravlev, V.A. Gritsenko, A.P. Yelissev, *J. Appl. Phys.* **116**, 244109 (2014)
51. R. Jiang, X. Du, W. Sun, Z. Han, Z. Wu, *Sci. Rep.* **5**, 15574 (2015)
52. C.E.L. Curtis, M. Doney, J.R. Johnson, *J. Am. Ceram. Soc.* **37**, 458–465 (1954)
53. J.A. Coppola, R.C. Bradt, *J. Am. Ceram. Soc.* **56**, 214–218 (1991)
54. H.J. Siebeneck, D.P.H. Hasselman, J.J. Cleveland, R.C. Bradt, *J. Am. Ceram. Soc.* **58**, 241–244 (1976)
55. H.P. Kirchner, R.M. Gruver, *J. Am. Ceram. Soc.* **53**, 232–236 (1970)
56. R. Materlik, C. Künneth, A. Kersch, *J. Appl. Phys.* **117**, 134109 (2015)
57. C. David, E. Nicolas, E. Azéma, *Comp. Geotech.* **67**, 150–156 (2015)
58. J.A. Astrom, H.J. Herrmann, *Eur. Phys. J. B* **5**, 551–554 (1998)